Acta Geodyn. Geomater., Vol. 23, No. 2 (222), 249–262, 2026
DOI: 10.13168/AGG.2026.0016

journal homepage: https://www.irsm.cas.cz/acta

ORIGINAL PAPER

GNSS VERTICAL TIME SERIES PREDICTION BASED ON THE INTEGRATION OF CEEMDAN-VMD-LSTM AND COMPOSITE ENTROPY

Tieding LU [1, 2, 4, 5, 6] *, Chen JIANG [2], Xiaoxing HE [3], Houming YANG [2] and Yuan ZHANG [2]

[1] Laboratory of Uranium Resource Exploration-Mining and Nuclear Remote Sensing, Nanchang 330013, China
[2] School of Surveying and Geoinformation Engineering, East China University of Technology, Nanchang, 330013, China
[3] School of Civil and Surveying and Mapping Engineering, Jiangxi University of Science and Technology, Ganzhou, 341000, China
[4] Key Laboratory of Mine Environmental Monitoring and Improving around Poyang Lake of Ministry of Natural Resources, East China University of Technology, Nanchang, 330013, China
[5] Jiangxi Key Laboratory of Watershed Ecological Process and Information (Platform No. 2023SSY01051), East China University of Technology, Nanchang, 330013, China
[6] Nanchang Key Laboratory of Landscape Process and Territorial Spatial Ecological Restoration, East China University of Technology,

**Corresponding author's e-mail:* tdlu@whu.edu.cn

ARTICLE INFO

Article history:
Received 22 October 2025
Accepted 11 April 2026
Available online 21 May 2026

Keywords:
GNSS vertical time series
Complete Ensemble Empirical Mode Decomposition with Adaptive Noise (CEEMDAN)
Variational Mode Decomposition (VMD)
Long Short-Term Memory (LSTM)
Prediction

ABSTRACT

GNSS vertical time series exhibit nonlinear and non-stationary characteristics, making it difficult for traditional time series forecasting methods to achieve high-precision predictions. To address this challenge, this study proposes a hybrid prediction model—CEEMDAN-VMD-LSTM—which integrates Complete Ensemble Empirical Mode Decomposition with Adaptive Noise (CEEMDAN), Variational Mode Decomposition (VMD), and Long Short-Term Memory (LSTM) networks. The model first applies the CEEMDAN algorithm to decompose the original GNSS time series into a set of Intrinsic Mode Functions (IMFs), and computes the Permutation Entropy (PE) and Sample Entropy (SE) of each IMF. A Composite Entropy (CE) is constructed by taking the equal-weighted average of PE and SE. Based on the composite entropy values, the K-Nearest Neighbors (KNN) algorithm is used to classify the IMFs into high-frequency and low-frequency components. These components are then linearly aggregated into high-frequency and low-frequency sequences, respectively. The high-frequency sequence undergoes a second decomposition using the VMD algorithm, resulting in k IMFs and a residual sequence. The low-frequency sequence (from the first decomposition), the IMFs, and the residual sequence (from the second decomposition) are separately modeled and predicted using the LSTM network. The final forecast is reconstructed by aggregating the predictions of the subcomponents. Experimental results on GNSS vertical time series from ten stations show that the proposed CEEMDAN-VMD-LSTM model achieves Root Mean Square Error (RMSE) values ranging from 2.20 mm to 3.69 mm, Mean Absolute Error (MAE) values between 1.75 mm and 2.95 mm, and coefficients of determination (R^2) ranging from 0.80 to 0.89. Compared with baseline models including LSTM, VMD-LSTM, CEEMDAN-VMD-RNN, and CEEMDAN-VMD-GRU, the proposed model demonstrates varying degrees of improvement, validating its effectiveness for GNSS vertical time series prediction.

1. INTRODUCTION

Over the past three decades, time series data recorded by more than 20,000 Global Navigation Satellite System (GNSS) reference stations worldwide have provided valuable foundational datasets for a wide range of Earth science studies (Jiang et al., 2018; Deng et al., 2017; Jiang et al., 2010). These GNSS station coordinate time series effectively capture long-term trends and nonlinear variations induced by geophysical processes (Zhu et al., 2020). Analyzing GNSS coordinate time series facilitates research in areas such as crustal plate motion (Dang et al., 2022; Yang et al. 2022; Gan et al. 2022), noise modeling and velocity estimation (Huang et al. 2025), engineering deformation monitoring (Xi et al., 2018; Jiang, Chen et al., 2022; Shi, 2023), maintenance of global and regional reference frames (Lahtinen et al., 2019; Sun et al., 2022; Jiang, Li et al., 2022), and inversion model construction (Bu et al., 2024; Yang, Yuan et al., 2024; He et al., 2023). Among the components of GNSS coordinate time series, the vertical component typically exhibits larger noise than the horizontal components, resulting in more complex variation characteristics and greater modeling difficulty. To characterize the complexity and nonlinearity of time series, researchers have introduced entropy-based measures from information theory, such as Permutation Entropy (PE) and Sample Entropy (SE). In the field of geodesy, these entropy metrics have been widely applied in studies such as GNSS coordinate time series noise analysis (Chen, Yang et al., 2023; Lu and Xie, 2021; Yang, Lu et al., 2024), seismic analysis (Xu et al., 2024), and signal extraction (Tao et al., 2024; Zhang et al., 2025). However, their application in the context of time series modeling and prediction remains relatively limited.

In recent years, with the rapid advancement of machine learning and deep learning techniques,

Cite this article as: Lu T, Jiang C, He X, Yang H, Zhang Y: GNSS vertical time series prediction based on the integration of CEEMDAN-VMD-LSTM and composite entropy**.** Acta Geodyn. Geomater., 23, No. 2 (222), 249–262, 2026. DOI: 10.13168/AGG.2026.0016

research on GNSS coordinate time series prediction based on artificial intelligence algorithms has received widespread attention. Researchers have employed various machine learning and deep learning models to conduct extensive studies on GNSS coordinate time series. For instance, (Gao et al., 2022) incorporated geophysical effects and utilized three models—Gradient Boosting Decision Tree (GBDT), Support Vector Machine (SVM), and Long Short-Term Memory (LSTM)—to model and predict GNSS station coordinate time series. (Jiao et al., 2025) proposed a hybrid AVMD-sLSTM-Transformer model, validated using over ten years of data from 584 GNSS stations worldwide. The method employs an improved adaptive variational mode decomposition (AVMD) and signal reconstruction to suppress noise. Results show that the model achieves sub-millimeter accuracy across all components, reducing prediction error by 65 % compared to sLSTM, improving by 32 % over the standard Transformer, and exceeding SVM and ARIMA by more than 80 % in MAE. Additionally, the model maintains residuals within ±1 mm for horizontal components, demonstrating excellent stability and adaptability. Li and Lu (2025) considered the spatial correlation between stations and applied the Adaptive Boosting (Adaboost) algorithm to model and predict GNSS stations in the Xinjiang region of China. Jiang et al. (2024) proposed a Deep Self-Attention Neural Network (DSANN) based on the Transformer framework for modeling and predicting GNSS coordinate time series in the same region. Wang et al. (2025) introduced an Enhancement Learning method based on Signal Source Driver (ELSSD), which integrates the strengths of both LSTM and DSANN while incorporating GNSS loading data as an auxiliary data source. Although machine learning and deep learning models based on artificial intelligence algorithms demonstrate strong learning capabilities in time series modeling, their performance can still be degraded when applied directly to raw time series data due to the presence of noise and complex trends. With the development of time series analysis, signal decomposition techniques have been widely applied to GNSS coordinate time series research to extract periodic components and primary trends (Li and Guo, 2024), while simultaneously suppressing noise. Common signal decomposition methods include Empirical Mode Decomposition (EMD), Ensemble Empirical Mode Decomposition (EEMD), Complete Ensemble Empirical Mode Decomposition with Adaptive Noise (CEEMDAN), and Variational Mode Decomposition (VMD). These methods are capable of decomposing complex time series into multiple Intrinsic Mode Functions (IMFs) or sub-signals at different scales, which contributes to enhanced predictive performance of subsequent models. Recent studies have already applied these methods in the field of surveying and mapping science (Lu et al., 2023; Lu et al., 2024; Zhou et al., 2025; Gong et al., 2024).

In existing studies, the decomposition–prediction–reconstruction strategy has been widely applied in nonlinear time series analysis (Chen, Lu, Huang, He and Sun, 2023). This strategy decomposes the original sequence into subcomponents with more homogeneous characteristics using signal decomposition methods. Each component is then predicted separately, and the final prediction is obtained by aggregating the forecasts of all components. This approach aims to enhance the prediction accuracy of complex signals. However, traditional decomposition methods such as Empirical Mode Decomposition (EMD) and Ensemble Empirical Mode Decomposition (EEMD) may suffer from mode mixing issues (Zhang et al., 2021). Moreover, these methods have not yet fully incorporated entropy analysis to quantify the complexity of each mode, which may result in inaccurate mode selection and classification, ultimately affecting the performance of subsequent prediction models.

Based on this, this study proposes a two-stage signal decomposition method that combines CEEMDAN and VMD. Composite Entropy (CE) is computed, and the K-Nearest Neighbors (KNN) algorithm is employed to classify the sub-modes. Finally, the Long Short-Term Memory (LSTM) network is used to perform the prediction.

2. PRINCIPLES AND METHODS

2.1. *COMPLETE ENSEMBLE EMPIRICAL MODE DECOMPOSITION WITH ADAPTIVE NOISE (CEEMDAN)*

Ensemble Empirical Mode Decomposition (EEMD) alleviates the mode mixing problem inherent in Empirical Mode Decomposition (EMD) by introducing auxiliary white noise. However, its decomposition accuracy depends on a high number of ensemble trials, which results in significant computational cost. To address this issue, Torres et al. proposed the Complete Ensemble Empirical Mode Decomposition with Adaptive Noise (CEEMDAN) algorithm in 2011 (Torres et al., 2011). CEEMDAN introduces adaptive white noise at each decomposition step and constructs a unique residual signal, thereby achieving lower reconstruction error with fewer ensemble trials. This method balances decomposition accuracy and computational efficiency. The specific decomposition procedure is as follows (Tang et al., 2021):

1. Construct the signal with added noise, which can be expressed by the following formula:

$$X_j(t) = X(t) + \varepsilon_0 \omega_j(t) \\ j = 1,2,\ldots,M \tag{1}$$

In Equation, $X_j(t)$ denotes the i-th noise-added signal, $X(t)$ represents the original signal, $\varepsilon_0$is the amplitude control coefficient of the white noise, $\omega_j(t)$ stands for the j-th independent white noise sequence, j is the current noise index, M indicates the total number of added noise ensembles, and *t* represents time or the sampling point.

2. Calculate the first Intrinsic Mode Function (IMF), which is expressed by the following formula:

$$IMF_1(t) = \frac{1}{N}\sum_{j=1}^{N} IMF_1^{(j)}(t) \tag{2}$$

In the formula, $IMF_1(t)$ denotes the resulting first *IMF* component, $IMF_1^{(j)}(t)$ represents the first IMF extracted from the j-th noise-added signal, and *N* is the number of ensemble averages.

3. Calculate the first-level residual, which is given by the following formula:

$$(t) = X(t) - IMF_1(t) \tag{3}$$

In Equation, r_1 represents the first-level residual, and $r_1(t)$ denotes the remaining part of the original signal after removing the first *IMF* component.

4. Add noise to the k-th level residual, which can be expressed by the following formula:

$$r_{k-1}^{(j)}(t) = r_{k-1}(t) + \varepsilon_{k-1} E_1(\omega_j(t)) \tag{4}$$

In the equation, $r_{k-1}^{(j)}(t)$ denotes the residual after adding auxiliary noise in the j-th ensemble, $r_{k-1}(t)$ represents the residual from the (k−1)-th level, ε_{k-1} is the amplitude control coefficient for the noise at this level, and $E(\omega_j(t))$ is the first IMF extracted from the j-th independent white noise using EMD.

5. Calculate the k-th Intrinsic Mode Function (IMF), which is expressed by the following formula:

$$IMF_k(t) = \frac{1}{N}\sum_{j=1}^{N} E_1\left(r_{k-1}^{(j)}(t)\right) \tag{5}$$

In Equation, $r_{k-1}^{(j)}(t)$ represents the k-th IMF component, N denotes the averaging number, and $E_1(r_{k-1}^{(j)}(t))$ indicates the first IMF extracted by EMD from the noise-added residual.

6. Update the residual, which is expressed by the following formula:

$$r_k(t) = r_{k-1}(t) - IMF_k(t) \tag{6}$$

In Equation, $r_k(t)$ denotes the updated residual signal, $r_{k-1}(t)$ represents the residual from the previous level, and $IMF_k(t)$ is the IMF obtained at the current iteration.

7. The final decomposition result of CEEMDAN is expressed as:

$$X(t) = \sum_{i=1}^{K} IMF_i(t) + \varsigma_k(t) \tag{7}$$

In Equation, *X(t)* represents the original signal, which is decomposed into *K* Intrinsic Mode Functions (IMFs), and $\varsigma_k(t)$ denotes the final residual, typically corresponding to a monotonic trend component.

2.2. VARIATIONAL MODE DECOMPOSITION (VMD)

Variational Mode Decomposition (VMD) is a signal processing method based on the principle of variational inference. It decomposes a signal into a set of Intrinsic Mode Functions (IMFs) with different center frequencies through an optimization process, effectively extracting the local time-frequency characteristics of the signal. This enables efficient signal decomposition and analysis. VMD iteratively solves a variational model to decompose the original time series into different mode components. The specific decomposition process is as follows (Humphrey et al., 1996):

1. Modulate the spectral components of each mode to their respective center frequencies and calculate the bandwidth. The squared L2 norm of the gradient for each mode is computed and demodulated using Gaussian smoothing:

$$\min_{\{\mu_k\},\{\omega_k\}} \left\{ \sum_k \left\| d_t \left[\left(\delta(t) + \frac{j}{\pi t} \right) * \mu_k(t) \right] * e^{-j\omega_k t} \right\|_2^2 \right\} \tag{8}$$

$$\mathrm{S}.\boldsymbol{t}.\ \sum_k \boldsymbol{\mu_k} = \boldsymbol{f} \tag{9}$$

In Equation, *t* represents time, $\delta(t)$ is the Dirac delta function, f denotes the original signal, μ_k is the mode function, ω_k represents the actual center frequency of each mode, and $e^{-j\omega_k t}$ is the estimated center frequency of each analytic signal. In Equation (9), $s.t.$ denotes the constraint term, $\sum_k \mu_k$ represents the summation over all mode components.

2. Based on this, a quadratic penalty factor α and a Lagrange multiplier operator λ_t are introduced to transform the constrained problem into an unconstrained variational problem. The Lagrangian functional is expressed as:

$$\begin{aligned} L(\{\mu_k\},\{\omega_k\},\lambda) = \\ \alpha \sum_k \left\| \partial_t \left[\left(\delta(t) + \frac{j}{\pi t} \right) * \mu_k(t) \right] e^{-j\omega_K t} \right\|_2^2 \\ + \left\| f(t) - \sum_k \mu_k(t) \right\|_2^2 \\ + \langle \lambda(t), f(t) - \textstyle\sum_k \mu_k(t) \rangle \end{aligned} \tag{10}$$

In Equation, α represents the quadratic penalty factor, λ_t denotes the Lagrange multiplier operator, and ∂_t is the partial derivative with respect to time. The unconstrained variational problem is solved using the Alternating Direction Method of Multipliers (ADMM). By alternately iterating $\mu_K^{n+1}, \omega_K^{n+1}, \lambda^{n+1}$, the saddle point of the augmented Lagrangian functional is obtained, which corresponds to the optimal solution of the constrained variational model in Equation (3).

2.3. COMPOSITE ENTROPY CALCULATION

Permutation Entropy (PE) and Sample Entropy (SE) are capable of reflecting the complexity of a signal. The detailed calculation procedure of

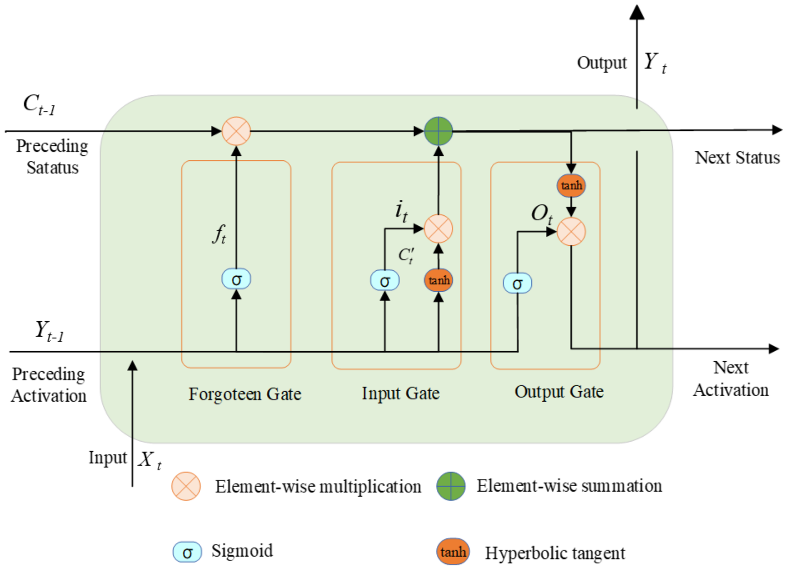

Fig. 1 LSTM structure diagram.

Permutation Entropy is as follows (Bandt and Pompe, 2002):

1. Given a time series $\{x_1, x_2, \dots, x_N\}$, set the embedding dimension *m* and time delay τ, and construct the embedding vectors as

$$X_i = (x_i, x_{i+\tau}, x_{i+2\tau}, \dots, x_{i+(m-1)\tau})$$
$$i = 1,2, \dots, N-(m-1)\tau \tag{11}$$

2. For each vector X_i, map it to a permutation pattern and calculate the probability distribution $\{p_1, p_2, \dots, p_k\}$ of all possible permutation patterns, where *k*=*m*. The Permutation Entropy is then computed based on this probability distribution:

$$PE = -\sum_{i=1}^{k} p_i \, log(p_i) \tag{12}$$

In the equation, PE represents the calculated Permutation Entropy value, *k* denotes the total number of possible permutation patterns, and p_i is the probability of occurrence of the permutation pattern *i*.

The detailed calculation procedure of Sample Entropy (SE) is as follows (Richman and Moorman, 2000):

1. Given a time series $\{x_1, x_2, \dots, x_N\}$, set the embedding dimension *m* and tolerance *r*, then construct the embedding vectors as follows:

$$u(i) = (x_i, x_{i+1}, \dots, x_{i+m-1})$$
$$i = 1,2, \dots, N-m+1 \tag{13}$$

2. Calculate the distances d between all vectors $u(i)$ and $u(j)$, which is expressed by the following formula:

$$d = |u(i) - u(j)| \tag{14}$$

3. If *d* is less than the tolerance *r*, the vectors are considered a match. Sample Entropy can then be calculated, which is expressed by the following formula:

$$SE(m, r, N) = -ln(\frac{B^{m+1}}{B^m}) \tag{15}$$

In Equation, B^m represents the number of matching m-dimensional vector pairs whose distances are less than r, Bm+1 denotes the number of matching (m+1)-dimensional vector pairs with distances less than r, N is the total number of epochs in the station data, and r is the tolerance.

The Composite Entropy (CE) is obtained by equally weighting and summing the Permutation Entropy (PE) and Sample Entropy (SE) of a single Intrinsic Mode Function (IMF), which is expressed by the following formula:

$$CE = aPE + bSE$$
$$a + b = 1$$
$$a = b \tag{16}$$

2.4. LONG SHORT-TERM MEMORY NETWORK (LSTM)

Long Short-Term Memory (LSTM) is an improved type of recurrent neural network proposed by Hochreiter and Schmidhuber (1997). Its unique memory cell architecture effectively addresses the long-term dependency problem inherent in traditional RNNs, while mitigating issues related to vanishing and exploding gradients. Compared to conventional neural networks, LSTM demonstrates significant advantages in handling long time series prediction tasks, which has led to its widespread application in the field of time series forecasting. The LSTM network architecture consists of an input layer, one or more hidden layers, and an output layer. Each hidden

Table 1 Site information table.

SITE	Longitude / °	Latitude / °	Missing Rate / %
AUCK	174.830	-36.603	1.6 %
CRO1	295.416	17.757	3.6 %
CORD	295.530	-31.528	2.1 %
FFMJ	8.665	50.091	1.5 %
HLFX	296.389	44.684	2.6 %
PTBB	52.296	10.460	1.0 %
TIDB	148.980	-35.399	1.8 %
WROC	51.113	17.062	3.6 %
WTZR	49.144	12.879	1.7 %
ZIMM	46.877	7.465	0.3 %

layer controls data storage and flow through three gates: the input gate, forget gate, and output gate. The structure is illustrated in Figure 1.

As shown in Figure 1, the LSTM processes the input time series data and the previous hidden state output through three gates. The detailed process is described in reference (Chen, Lu, Huang, He, Yu et al., 2023):

1. The LSTM uses the forget gate f_t to determine whether to discard or retain the relevant information of X_t and Y_{t-1}, with the activation state of the forget gate determined by the activation function σ.

$$f_t = \sigma(W_f \cdot [Y_{t-1}, X_t] + b_f) \tag{17}$$

In the formula, W and b represent the weight matrix and bias, respectively. f_t is a vector with values ranging from 0 to 1, indicating whether the information in the cell state C_{t-1} should be retained. A value of 0 means the information is discarded, while a value of 1 means it is retained.

2. The cell state is updated through the input gate, where X_t and Y_{t-1} are passed to the activation function σ to determine the information to be updated. Then, X_t and Y_{t-1} are passed to the *tanh* function to create a new candidate value vector C'_t (with values ranging from –1 to 1). Finally, the output of the tanh function is multiplied by the output value of σ.

$$i_t = \sigma(W_i \cdot [Y_{t-1}, X_t] + b_i)$$
$$C'_t = tanh(W_c \cdot [Y_{t-1}, X_t] + b_c) \tag{18}$$

The cell state from the previous layer is element-wise multiplied by the forget vector, and the result is then element-wise added to the output of the input gate to obtain the updated cell state.

$$C_t = f_t * C_{t-1} + i_t * C'_t \tag{19}$$

In Equation, $f_t * C_{t-1}$ determines which information in C_{t-1} should be forgotten, while $i_t * C'_t$ determines which information in C'_t should be added to the new memory cell state C_t.

3. The output gate O_t determines the value of the next hidden state Y_t, which contains information from previous inputs.

$$O_t = \sigma(W_O \cdot [Y_{t-1}, X_t] + b_O)$$
$$Y_t = O_t * tanh(C_t) \tag{20}$$

In Equation, W_O represents the weight matrix of the output gate, and b_O denotes the bias vector, both of which can be obtained through training.

2.5. *EVALUATION METRICS*

To verify the accuracy and reliability of the model's predictions, this experiment uses Root Mean Square Error (RMSE) and Mean Absolute Error (MAE) as evaluation metrics. The calculation formulas are as follows:

1. Root Mean Square Error (RMSE)

$$RMSE = \sqrt{\frac{1}{n}\sum_{i=1}^{n}(y_i - \hat{y}_i)^2} \tag{21}$$

2. Mean Absolute Error (MAE)

$$MAE = \frac{1}{n}\sum_{i=1}^{n}|(y_i - \hat{y}_i)| \tag{22}$$

3. Coefficient of Determination (R^2)

$$R^2 = 1 - \frac{\sum_{i=1}^{n}(y_i - \hat{y}_i)^2}{\sum_{i=1}^{n}(y_i - \bar{y})^2} \tag{23}$$

In Equations, y_i represents the actual coordinate values, $\hat{y}_i$ denotes the predicted values from each model, $\bar{y}$ is the mean of the actual coordinate values, and n is the total number of relevant data points. For RMSE and MAE, smaller values indicate higher prediction accuracy. For R^2, an absolute value closer to 1 indicates better fitting performance, while a value closer to 0 signifies weaker explanatory power of the model.

3. DATA AND EXPERIMENTS

In this study, 10 daily GNSS vertical time series from 2014 to 2023, with uncorrected offsets, were selected from the Scripps Orbit and Permanent Array Center (SOPAC, available at https://sopac-csrc.ucsd.edu/index.php/sopac/) for experiments.

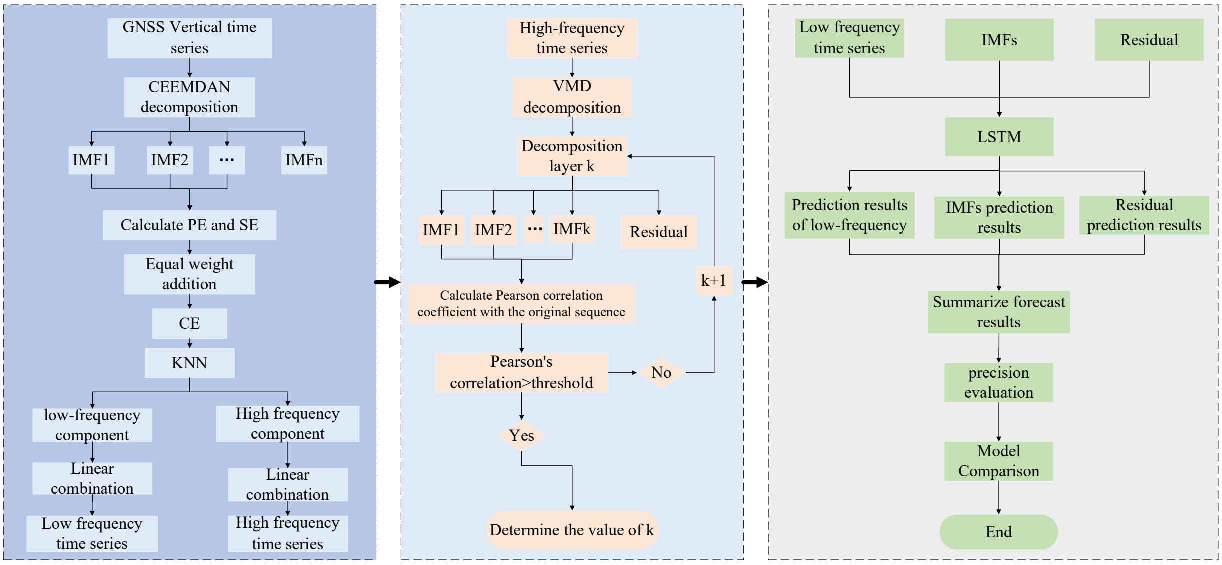

Fig. 2 Flow chart of model construction.

GNSS station data often contain a certain amount of outliers, as well as missing values caused by events such as earthquakes or equipment replacement. In this paper, the 3-sigma outlier detection method is first applied to identify and remove outliers. Since the missing data rate for all 10 stations is below 5%, indicating a relatively low level of missingness, linear interpolation is used to fill the missing values in order to preserve the original linear trend of the series as much as possible (Lu et al., 2024). The information on the test stations and their corresponding missing data rates is shown in Table 1.

The experimental setup of this study is as follows: After preprocessing, the 3,652 daily solution epochs were divided into three subsets. The first 2,556 data points were used as the training set to train the model parameters and learn the underlying data features. The subsequent 365 data points were used as the validation set for hyperparameter tuning and model performance evaluation. The remaining 731 data points constituted the test set for assessing the overall predictive performance of the model. To ensure consistency in the modeling process, the training set, validation set, and test set were all decomposed using the CEEMDAN-VMD method before being input into the prediction model.

To verify the prediction performance of the CEEMDAN-VMD-LSTM model, this study set up several comparative models, including LSTM, VMD-LSTM, CEEMDAN-VMD-GRU, and CEEMDAN-VMD-RNN. Prior to the experiments, parameter tuning was conducted for all models to ensure consistency of related parameters in the comparative process. The specific parameters include: a learning rate of 0.001, 50 training epochs, a sliding window size of 10, an input feature dimension of 1, an output feature dimension of 1, and a hidden layer size of 256.

The sliding window size of 10 indicates that ten consecutive historical observations are used as input to predict the value at the next time step. Since the GNSS vertical time series in this study is a univariate sequence, the input feature dimension is set to 1, meaning that each time step contains only one feature value. The output feature dimension of 1 indicates that the model predicts a single value for the next epoch. The hidden layer size of 256 means that the LSTM network contains 256 neurons in the hidden layer, which enhances the model's ability to capture complex nonlinear temporal dependencies in the time series. During the prediction stage, a step-by-step prediction strategy is adopted. Specifically, the trained model first uses the most recent ten observations as input to predict the next value, and the predicted value is then incorporated into the sequence to construct a new input window for subsequent predictions, thereby achieving continuous prediction of the time series.

3.1. MODEL CONSTRUCTION

The original time series data is first decomposed using CEEMDAN to obtain a set of Intrinsic Mode Functions (IMFs). For each IMF, both permutation entropy and sample entropy are calculated. These two entropy measures are then equally weighted and summed to obtain the composite entropy. Based on the composite entropy values, the IMFs are clustered into high-frequency and low-frequency groups using the K-Nearest Neighbors (KNN) algorithm. The high-frequency and low-frequency IMFs are then linearly summed to form a high-frequency sequence and a low-frequency sequence, respectively. The high-frequency sequence is further decomposed using the Variational Mode Decomposition (VMD) algorithm to extract finer-scale features. Subsequently, the decomposed sub-modes from VMD, the residual sequence, and the low-frequency sequence are all input into the LSTM network for prediction. This forms a second-level hybrid prediction model, referred to as CEEMDAN-

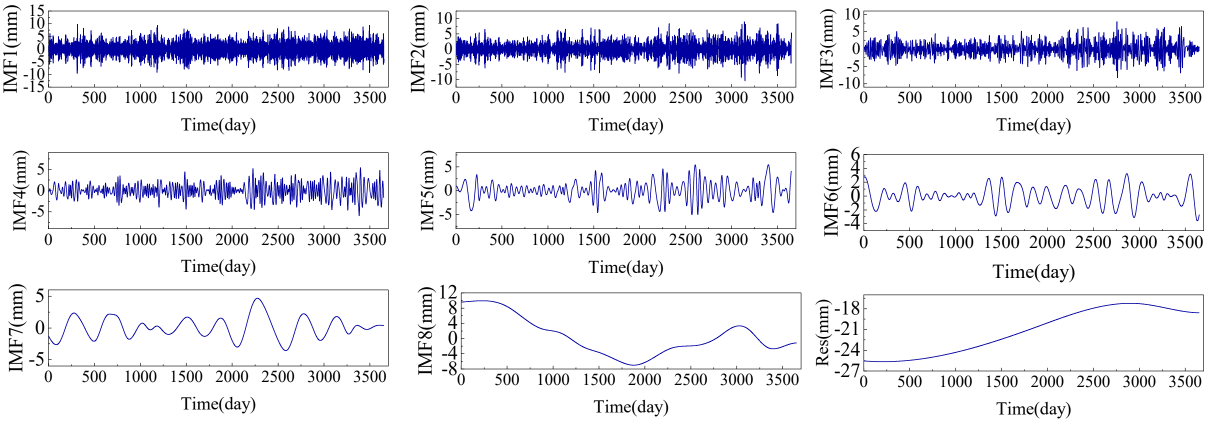

Fig. 3 CEEMDAN decomposition results of AUCK station elevation time series.

VMD-LSTM. The overall modeling process is illustrated in Figure 2.

The specific process of the prediction model proposed in this study is as follows:

Step 1: The CEEMDAN algorithm is applied to the GNSS vertical time series for initial decomposition, resulting in several Intrinsic Mode Functions (IMFs).

Step 2: The permutation entropy and sample entropy of each IMF are calculated, and their equally weighted sum is taken to obtain the composite entropy.

Step 3: Use the K-Nearest Neighbors (K-NN) clustering algorithm to classify the IMFs into high-frequency and low-frequency signals based on the composite entropy, then linearly superimpose the components of the high-frequency and low-frequency signals to obtain the reconstructed high-frequency and low-frequency sequences.

Step 4: Apply the Variational Mode Decomposition (VMD) algorithm to further decompose the high-frequency signal. The decomposition parameter k is determined by calculating the Pearson correlation coefficient between the reconstructed data and the original data.

Step 5: Input the Intrinsic Mode Functions (IMFs) and residual sequence obtained from VMD decomposition, along with the low-frequency sequence, separately into the LSTM model for prediction.

Step 6: Linearly superimpose the prediction results of the low-frequency signals, the secondary decomposed sub-modes, and the residual sequences from each model to obtain the aggregated reconstruction.

Step 7: Calculate the errors and perform accuracy evaluation.

3.2. CEEMDAN DECOMPOSITION

The experiment first applies the CEEMDAN algorithm to decompose the raw data. CEEMDAN adaptively decomposes the original data into several Intrinsic Mode Functions (IMFs) and a residual term representing the trend. The decomposition results are shown in Figure 3, taking the AUCK station as an example. As illustrated in Figure 3, IMF1 to IMF3 exhibit rapid oscillations with small amplitudes and short periods, reflecting fast changes on a short time scale. IMF4 and IMF5 also display rapid oscillations but with lower frequencies than IMF1 to IMF3. IMF6 to IMF9 show gentle trends or long-period fluctuations with larger amplitudes and longer periods, which may include signals caused by geophysical effects such as annual, semi-annual cycles or long-term trends. The residual term (Res) represents a single monotonic trend component.

3.3. ENTROPY CALCULATION AND SIGNAL CLASSIFICATION

Entropy is commonly used to characterize the complexity and randomness of time series. In this study, the permutation entropy and sample entropy of each Intrinsic Mode Function (IMF) obtained from CEEMDAN decomposition were calculated. The permutation entropy and sample entropy were then equally weighted and summed to compute the Composite Entropy (CE), which serves as a comprehensive measure of the information complexity of each component.

Since the Intrinsic Mode Functions (IMFs) obtained from CEEMDAN decomposition exhibit different spectral characteristics, to more clearly distinguish between high-frequency and low-frequency signals, this study employs the K-Nearest Neighbors (KNN) algorithm to classify the IMFs. The KNN algorithm automatically partitions the IMFs into high-frequency and low-frequency signals based on their composite entropy values. Taking the AUCK station as an example, the calculated entropy values and classification results are shown in Table 2.

Based on the KNN classification results, the classified low-frequency and high-frequency signals are linearly superimposed separately to obtain the reconstructed high-frequency and low-frequency time series. The reconstructed time series for the experimental stations based on high- and low-frequency components are shown in Figure 4, with four representative stations illustrated as examples. In Figure 4, the light blue curves represent the high-

Table 2 Calculation results and signal classification of composite entropy of AUCK station.

IMFs	PE	SE	CE	Classification Results
IMF1	0.999769	0.683745	0.841757	High frequency signal
IMF2	0.876864	0.682199	0.779532	High frequency signal
IMF3	0.704240	0.680574	0.692407	High frequency signal
IMF4	0.569012	0.684001	0.626507	High frequency signal
IMF5	0.482052	0.675714	0.578883	High frequency signal
IMF6	0.436815	0.679897	0.558356	Low frequency signal
IMF7	0.409389	0.681329	0.545359	Low frequency signal
IMF8	0.389023	0.656251	0.522637	Low frequency signal
IMF9	0.234453	0.636877	0.480665	Low frequency signal

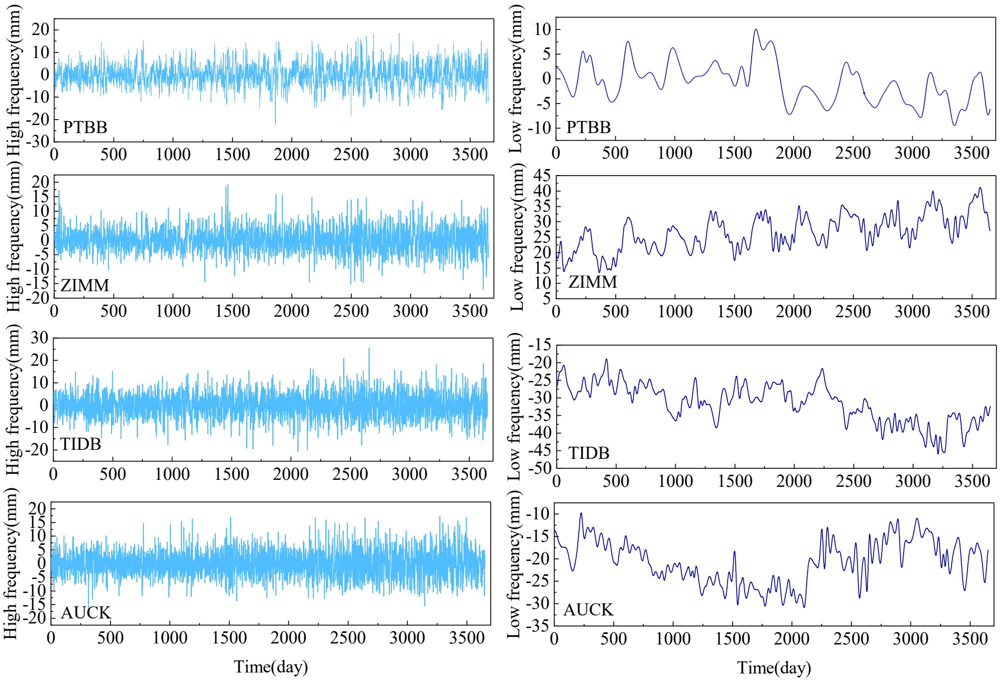

(a)Stacked high-frequency signal (b)Stacked low-frequency signal

Fig. 4 Superimposed high and low frequency signals.

frequency time series reconstructed by superimposing the high-frequency signals, while the dark blue curves represent the low-frequency time series reconstructed by superimposing the low-frequency signals. From Figure 4, it can be observed that the superimposed high-frequency time series mainly exhibit short-period rapid fluctuations with small amplitude and frequent changes. In contrast, the superimposed low-frequency time series mainly display stable trend-like variations with larger amplitude fluctuations.

3.4. VMD DECOMPOSITION OF DATA

When using VMD for data decomposition, selecting the number of IMF components k is crucial. A too small k leads to under-decomposition of modes, while a too large k may cause mode mixing or introduce additional noise (Wu et al., 2024). Luo et al. (2020) consider correlation coefficients less than 0.1 as criteria for removing false and noise components. In this study, the Pearson correlation coefficients between the linear superposition of the decomposed IMFs and the original sequence are calculated. A threshold of 0.9 is set to select reconstructed sequences with correlation coefficients above 0.9, thereby determining the optimal value of k.

The original data from the experimental stations are decomposed using the VMD algorithm. The resulting Intrinsic Mode Functions (IMFs) and residual components are then input into the LSTM model to construct the VMD-LSTM model for comparative experiments. The VMD decomposition process for the high-frequency signals follows the same procedure as that for the original data. The selected values of k for the decompositions are listed in Table 3.

3.5. VMD-LSTM FIRST-ORDER PREDICTION MODEL

To validate the effectiveness of the proposed two-stage decomposition model, this study first introduces the first-order decomposition model VMD-

Table 3 k value of VMD decomposed high frequency signal.

Site	VMD decomposition of high-frequency signals		VMD decomposition of raw signal	
	Pearson's correlation	k	Pearson's correlation	k
AUCK	0.9097	8	0.9086	7
CORD	0.9057	8	0.9171	7
CRO1	0.9010	8	0.9040	6
FFMJ	0.9200	8	0.9052	6
HLFX	0.9143	8	0.9206	8
PTBB	0.9113	7	0.9122	6
TIDB	0.9062	8	0.9190	7
WROC	0.9041	7	0.9193	6
WTZR	0.9059	7	0.9183	6
ZIMM	0.9020	7	0.9216	5

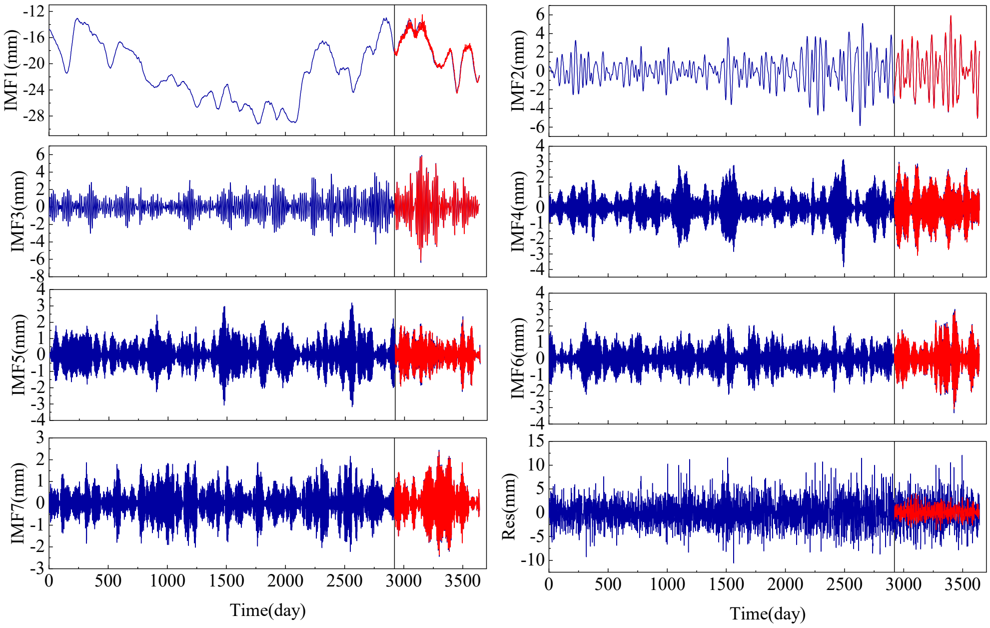

Fig. 5 VMD decomposition results of original data.

LSTM for comparative experiments. The VMD algorithm decomposed the original time series data from the PTBB station into six Intrinsic Mode Functions (IMFs) and one residual sequence. The decomposition and prediction results are shown in Figure 5.

As shown in Figure 5, IMF1 to IMF6 represent signal components with different frequencies. Each IMF corresponds to a specific frequency range, capturing fluctuations at various time scales. The lower-frequency IMFs contain long-term trend variations in the signal, while the higher-frequency IMFs reflect short-term fluctuations and noise. IMF1 is the lowest-frequency component, potentially representing long-term trends such as annual cycles. IMF2 also has a relatively low frequency and may correspond to semi-annual or seasonal variations caused by geophysical effects or climate changes. IMFs 3 to 7 exhibit higher fluctuation frequencies, reflecting short-term variations in the signal, possibly representing high-frequency noise and similar components. The residual component generally reflects more complex or irregular parts of the signal.

In Figure 5, the dark blue curves represent the individual Intrinsic Mode Functions (IMFs) and the residual sequence, while the red curve shows the fitting results of the LSTM model. It can be observed that IMF1 to IMF6 have good fitting accuracy, maintaining similar fluctuations and trends as the original sequence with no significant differences. The fitting errors are mainly concentrated in the residual sequence, where the model performs poorly and errors are relatively large. This is likely because the residual sequence lacks obvious regularity and clear statistical features, making it difficult for the model to learn effectively.

3.6. CEEMDAN-VMD-LSTM TWO-STAGE PREDICTION MODEL

The linearly superimposed high-frequency signal of the AUCK station was further decomposed by VMD into 8 Intrinsic Mode Functions (IMFs) and 1

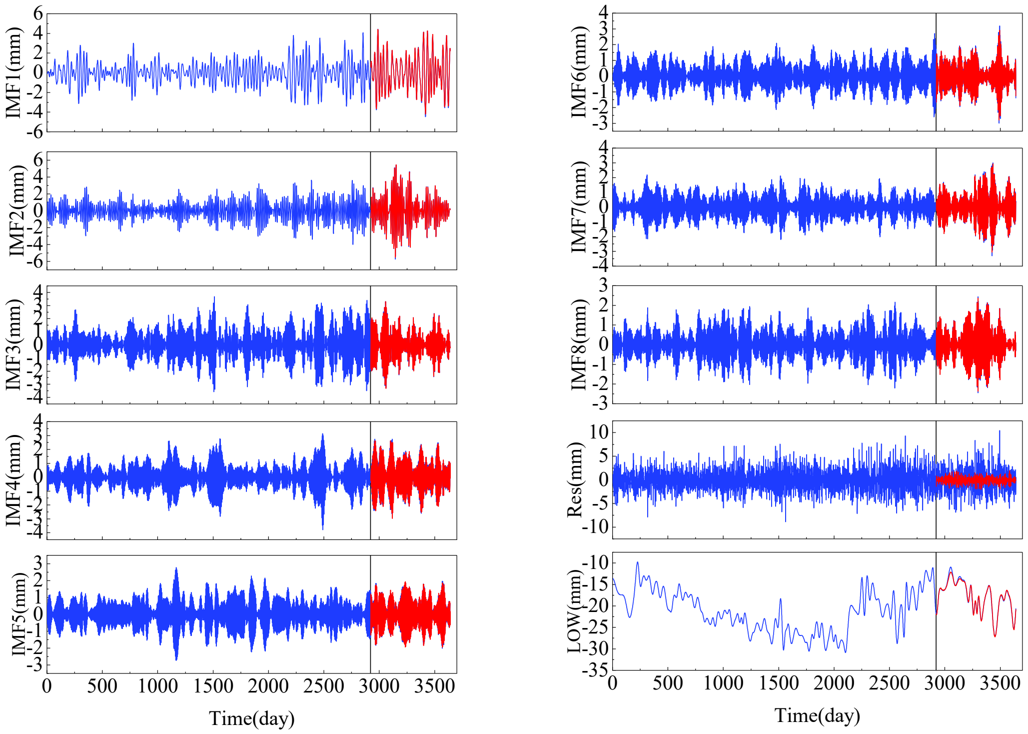

Fig. 6 Prediction results of CEEMDAN-VMD-LSTM model.

residual component. These, along with the low-frequency sequence, were input into the LSTM model to construct the CEEMDAN-VMD-LSTM two-stage hybrid prediction model. The decomposition and prediction results are shown in Figure 6.

As shown in Figure 6, the decomposition resulted in 8 IMFs and 1 residual sequence, with each IMF representing a frequency band component of the signal. From IMF1 to IMF8, these intrinsic mode functions correspond to signal components within different frequency ranges. For example, the first IMF may contain lower-frequency fluctuations, while IMF8 likely contains high-frequency components, reflecting rapid oscillations or noise. The residual component generally represents more complex or irregular parts of the signal.

In Figure 6, the blue curves represent the Intrinsic Mode Functions (IMFs) and residual sequence obtained from the VMD decomposition of the high-frequency signal, while the red curves show the LSTM model's fitting results. It can be observed that the fitting of IMF1 through IMF8 closely matches the original sequence. The overall fitting of the low-frequency signal is good, although there is a poorer fit between epochs 3100 and 3250. This may be because this segment corresponds to a peak region in the sequence, where the model struggles to accurately capture the fluctuation trend. However, the low-frequency sequence fits well overall. The fitting errors are mainly concentrated in the residual sequence.

3.7. PREDICTION RESULTS OF DIFFERENT MODELS

To evaluate the prediction performance of the proposed CEEMDAN-VMD-LSTM hybrid model, comparative experiments were designed. The models compared include the single LSTM model, the first-order decomposition combination model VMD-LSTM, and two other second-order decomposition combination models, CEEMDAN-VMD-GRU and CEEMDAN-VMD-RNN. In this study, the Intrinsic Mode Functions (IMFs) and residuals obtained from the VMD decomposition of the original data were input into the LSTM model to construct the VMD-LSTM model. Similarly, the second-stage decomposed IMFs, low-frequency sequences, and residual sequences were separately fed into the GRU and RNN models to build the CEEMDAN-VMD-GRU and CEEMDAN-VMD-RNN two-stage combination models. The prediction results of the components from each model were linearly combined following a "decomposition–prediction–reconstruction" procedure, yielding overall prediction values for LSTM, VMD-LSTM, CEEMDAN-VMD-LSTM, CEEMDAN-VMD-GRU, and CEEMDAN-VMD-RNN models. By comparing with the original sequence, the differences in prediction accuracy and fitting performance among these models were further analyzed. The prediction curves for LSTM, VMD-LSTM, and CEEMDAN-VMD-LSTM models are shown in Figure 7(a), while the prediction curves for CEEMDAN-VMD-RNN, CEEMDAN-VMD-GRU, and CEEMDAN-VMD-LSTM models are shown in Figure 7(b).

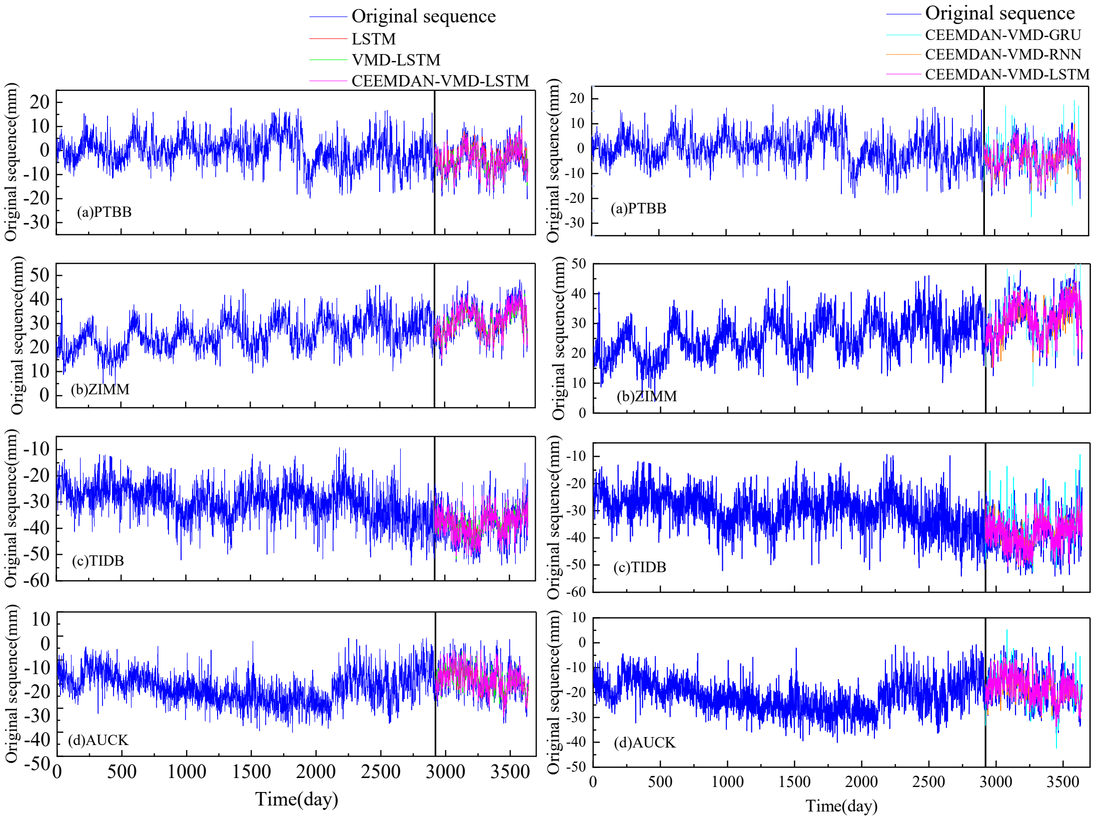

(a) (b)

Fig. 7 Summary of prediction results of different combination models.

In Figure 7(a), the blue curve represents the original sequence, the red curve shows the prediction results of the single LSTM model, the green curve corresponds to the VMD-LSTM model predictions, and the magenta curve indicates the predictions from the CEEMDAN-VMD-LSTM model. It can be observed from Figure 7(a) that the single LSTM model exhibits relatively poor fitting performance across the four stations. In contrast, the fitting curves of the VMD-LSTM and CEEMDAN-VMD-LSTM models are much closer to the original sequences, demonstrating better fitting quality. Among them, the CEEMDAN-VMD-LSTM model best captures the fluctuations and trends of the original sequences, achieving the overall best fitting performance.

Figure 7(b) shows the fitting results of the three second-order hybrid prediction models. In Figure 7(b), the cyan curve represents the prediction results of the CEEMDAN-VMD-GRU model, the orange curve represents the CEEMDAN-VMD-RNN model predictions, and the magenta curve corresponds to the CEEMDAN-VMD-LSTM model predictions. Among these, the CEEMDAN-VMD-GRU model exhibits noticeable deviations and unsatisfactory prediction performance. The CEEMDAN-VMD-RNN model's fitting is closer to the original sequence, showing relatively good prediction results. The CEEMDAN-VMD-LSTM model best maintains consistency with the fluctuations and trends of the original sequence, achieving the overall best fitting performance.

Figure 8 and Table 4 present the statistical charts of the three evaluation metrics for the prediction results of each model across the 10 stations.

As shown in Figure 8 and Table 4, the LSTM model's prediction errors have RMSE values ranging from 4.28 mm to 7.92 mm, MAE values ranging from 3.36 mm to 6.46 mm, and R^2 values between 0.06 and 0.61, with relatively poor fitting performance at some stations due to low R^2 values. The VMD-LSTM model achieves RMSE values between 2.85 mm and 3.90 mm, MAE values between 2.23 mm and 3.10 mm, and R^2 values from 0.72 to 0.84. The CEEMDAN-VMD-GRU model's RMSE ranges from 3.57 mm to 5.36 mm, MAE from 2.53 mm to 3.77 mm, and R^2 between 0.45 and 0.71. The CEEMDAN-VMD-RNN model records RMSE values between 2.91 mm and 4.23 mm, MAE between 2.31 mm and 3.26 mm, and R^2 values from 0.72 to 0.81. The CEEMDAN-VMD-LSTM model achieves the best performance with RMSE values ranging from 2.20 mm to 3.69 mm, MAE values from 1.75 mm to 2.95 mm, and R^2 values as high as 0.80 to 0.89.

As shown in Table 4, the CEEMDAN-VMD-LSTM model outperforms the other comparison models on three evaluation metrics—RMSE, MAE, and R^2—across the 10 GNSS stations. Compared to the LSTM, VMD-LSTM, CEEMDAN-VMD-GRU, and CEEMDAN-VMD-RNN models, the RMSE values of the CEEMDAN-VMD-LSTM model decrease by 44.9 %-52.9 %, 3.4 %-28.8 %, 27.5 %-

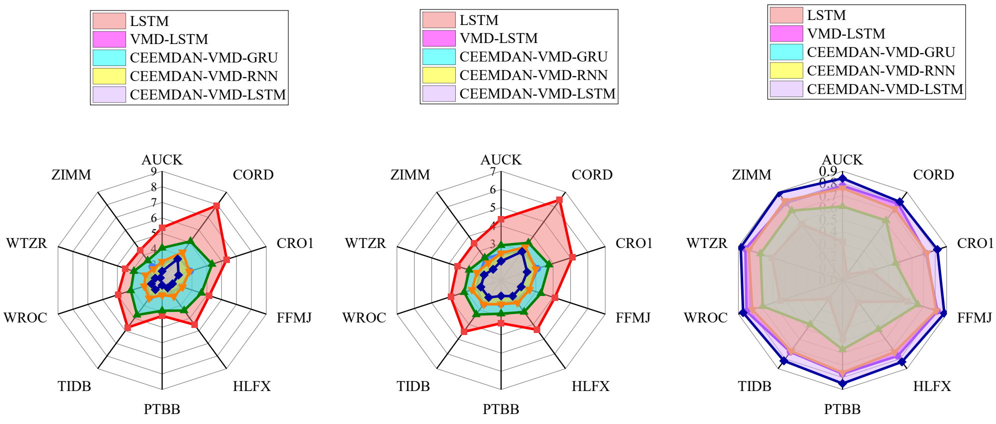

(a)RMSE (b)MAE (c)R^2

Fig. 8 Statistical chart of prediction results of different models.

Table 4 Prediction results of different models at the test site.

Site	Evaluation /mm	LSTM	VMD-LSTM	CEEMDAN-VMD-GRU	CEEMDAN-VMD-RNN	CEEMDAN VMD-LST
	RMSE	5.38	3.06	4.08	3.21	2.59
AUCK	MAE	4.37	2.44	2.93	2.50	2.05
	R^2	0.32	0.78	0.61	0.76	0.84
	RMSE	7.92	3.82	5.09	4.23	3.69
CORD	MAE	6.46	3.01	3.55	3.26	2.95
	R^2	0.06	0.78	0.61	0.73	0.80
	RMSE	6.34	3.90	5.36	3.83	3.10
CRO1	MAE	5.10	3.10	3.77	3.00	2.50
	R^2	0.25	0.72	0.46	0.73	0.82
	RMSE	5.17	3.27	4.64	3.38	2.70
FFMJ	MAE	4.09	2.60	3.30	2.64	2.16
	R^2	0.56	0.82	0.65	0.81	0.88
	RMSE	5.52	2.99	4.39	3.27	2.60
HLFX	MAE	4.35	2.38	3.15	2.53	2.07
	R^2	0.22	0.77	0.50	0.73	0.83
	RMSE	4.28	2.90	3.95	2.94	2.31
PTBB	MAE	3.36	2.31	2.83	2.31	1.86
	R^2	0.49	0.77	0.57	0.76	0.85
	RMSE	5.74	3.34	4.74	3.41	2.74
TIDB	MAE	4.49	2.61	3.32	2.63	2.16
	R^2	0.19	0.73	0.45	0.72	0.82
	RMSE	4.97	3.02	4.11	3.42	2.72
WROC	MAE	3.90	2.42	3.13	2.68	2.17
	R^2	0.54	0.83	0.69	0.78	0.86
	RMSE	4.48	2.85	3.90	3.11	2.47
WTZR	MAE	3.53	2.23	2.84	2.40	1.98
	R^2	0.61	0.84	0.71	0.81	0.88
	RMSE	4.39	3.09	3.57	2.91	2.20
ZIMM	MAE	3.52	2.49	2.53	2.18	1.75
	R^2	0.57	0.79	0.71	0.81	0.89

42.2 %, and 12.8 %-24.4 %, respectively, indicating that the CEEMDAN-VMD-LSTM model achieves higher overall prediction accuracy and greater stability than these four comparison models. The MAE values of the CEEMDAN-VMD-LSTM model are reduced by 43.9 %-54.3 %, 2 %-29.7 %, 16.9 %-34.9 %, and 9.5 %-19.7 % compared to the four models, respectively, demonstrating that it more effectively reduces prediction bias and offers higher prediction accuracy. Regarding R^2, the CEEMDAN-VMD-LSTM model improves by 30.7 %-92.5 %, 2.5 %-12.2 %, 19.0 %-45.1 %, and 8.0 %-12.2 % compared to the four models, respectively, indicating superior fitting performance relative to the other models.

4. CONCLUSION

This study employs CEEMDAN and VMD decomposition algorithms to perform secondary decomposition of GNSS vertical time series data from 10 stations based on composite entropy. The resulting intrinsic mode functions, low-frequency signals, and residual sequences are separately input into an LSTM network to construct the CEEMDAN-VMD-LSTM model. The following conclusions are drawn:

1. The proposed CEEMDAN-VMD-LSTM second-order decomposition hybrid model demonstrates excellent performance in vertical time series prediction. Experimental results from 10 GNSS stations show that the CEEMDAN-VMD-LSTM model outperforms both the single LSTM model and the first-order VMD-LSTM hybrid model in terms of RMSE, MAE, and R^2 metrics, validating the effectiveness of the second-order decomposition approach.
2. Compared with other second-order hybrid models, CEEMDAN-VMD-GRU and CEEMDAN-VMD-RNN, the CEEMDAN-VMD-LSTM model demonstrates significant advantages in stability, prediction accuracy, and fitting performance. This indicates that the combination of the LSTM model with the second-order decomposition method is more effective in handling the nonlinear and non-stationary characteristics of GNSS vertical time series data.
3. This study validates the feasibility and advantages of the "decomposition–prediction–reconstruction" hybrid modeling framework for non-stationary time series. By combining signal decomposition methods with prediction models, predicting each decomposed sub-mode separately, and aggregating the prediction results, the forecasting performance can be effectively improved.

REFERENCES

Bandt, C. and Pompe, B.: 2002, Permutation entropy: a natural complexity measure for time series. Phys. Rev. Lett., 88, 174102. DOI: 10.1103/PhysRevLett.88.174102

Bu, J., Yu, K., Wang, Q., Li, L., Liu, X., Zuo, X. and Chang, J.: 2024, Deep learning inversion method for global ocean effective wave height based on integration of spaceborne GNSS-R data and multivariate parameters. Acta Geod. Cartogr. Sin., 53, 7, 1321–1335, (in Chinese). DOI: 10.11947/j.AGCS.2024.20230050

Chen, H., Lu, T., Huang, J., He, X. and Sun, X.: 2023, An improved VMD–EEMD–LSTM time series hybrid prediction model for sea surface height derived from satellite altimetry data. J. Mar. Sci. Eng., 11, 12, 2386. DOI: 10.20944/preprints202310.1457.v1

Chen, H., Lu, T., Huang, J., He, X., Yu, K., Sun, X., Ma, X. and Huang, Z.: 2023, An improved VMD-LSTM model for time-varying GNSS time series prediction with temporally correlated noise. Remote Sens., 15, 14, 3694. DOI: 10.3390/rs15143694

Chen, X., Yang, Z., Tian, Z., Yang, B. and Liang, P.: 2023, Denoising method for GNSS time series based on GA-VMD and multi-scale permutation entropy. Geomat. Inf. Sci. Wuhan Univ., 48, 9, 1425–1434, (in Chinese). DOI: 10.13203/j.whugis20210215

Dang, Y., Yang, Q., Wang, W. and Liang, Y.: 2022, Three-dimensional crustal tectonic deformation analysis of the Tibetan Plateau and its adjacent areas based on a block model. Acta Geod. Cartogr. Sin., 51, 7, 1192–1205, (in Chinese). DOI: 10.11947/j.AGCS.2022.20220123

Deng, L., Jiang, W., Li, Z., Chen, H., Wang, K. and Ma, Y.: 2007, Assessment of second-and third-order ionospheric effects on regional networks: case study in China with longer CMONOC GPS coordinate time series. J. Geod., 91, 2, 207–227. DOI: 10.1007/s00190-016-0957-y

Gan, W., Molnar, P., Zhang, P., Xiao, G., Liang, S., Zhang, K., Li, Z., Xu, K. and Zhang. L.: 2022, Initiation of clockwise rotation and eastward transport of southeastern Tibet inferred from deflected fault traces and GPS observations. Geol. Soc. Am. Bull., 134, 5-6, 1129–1142. DOI: 10.1130/B36069.1

Gao, W., Li, Z., Chen, Q., Jiang, W. and Feng, Y.: 2022, Modelling and prediction of GNSS time series using GBDT, LSTM and machine learning approaches. J. Geod., 96, 10, 71. DOI: 10.1007/s00190-022-01662-5

Gong, X., Qiu, W., Lv, K., Zhang, T., Zhang, R. and Luo, S.: 2024, Variational mode decomposition and adaptive graph convolutionateal gated recurrent network for traffic flow combination prediction model. Geomat. Inf. Sci. Wuhan Univ., 49, 12, 2329–2341, (in Chinese). DOI: 10.13203/j.whugis20230249

He, R.J., Zheng, N., Ding, R., Zhang, K. and Chen, T.: 2023, Soil moisture inversion method based on particle swarm optimized convolutional neural network using GNSS-IR. Acta Geod. Cartogr. Sin., 52, 8, 1286–1297, (in Chinese). DOI: 10.11947/j.AGCS.2023.20220277

Hochreiter, S. and Schmidhuber, J.: 1997, Long short-term memory. Neural Comput., 9, 8, 1735–1780. DOI: 10.1162/neco.1997.9.8.1735

Huang, J., He, X., Hu, S. and Ming, F.: 2025, Impact of offsets on GNSS time series stochastic noise properties and velocity estimation. Adv. Space Res., 75, 4, 3397–3413. DOI: 10.1016/j.asr.2024.12.016

Humphrey, W., Dalke, A. and Schulten, K.: 1996, VMD: visual molecular dynamics. J. Mol. Graph., 14, 1, 33–38. DOI: 10.1016/0263-7855(96)00018-5

Jiang, W.., Chen, Y., Chen, Q., Chen, H., Pan, Y., Liu, X. and Liu, T.: 2022, High precision deformation monitoring with integrated GNSS and ground range observations in harsh environment. Measurement, 204, 112179. DOI: 10.1016/j.measurement.2022.112179

Jiang, W., Li, Z., Liu, W. and Zhou, X.: 2010, Some thoughts on establishment and maintenance of terrestrial reference frame considering non-linear variation. Geomat. Inf. Sci. Wuhan Univ., 35, 6, 665–669. DOI:10.13203/j.whugis2010.06.006

Jiang, W., Li, Z., Wei, N. and Liu, J.: 2022, Progress and thinking on the establishment of geodetic coordinate framework. Acta Geod. Cartogr. Sin., 51, 7, 1259–1270, (in Chinese). DOI: 10.11947/j.AGCS.2022.20220232

Jiang, W, Wang, J., Li, Z., Li, W. and Yuan, P.: 2024, A new deep self-attention neural network for GNSS coordinate time series prediction. GPS Solut., 28, 1. DOI: 10.1007/s10291-023-01544-z

Jiang, W., Wang, K., Li, Z., Zhou, X., Ma, Y. and Ma, J.: 2018, Theory, methods, and prospects of GNSS coordinate time series analysis. Geomat. Inf. Sc. Wuhan Univ., 43, 12, 2112–2123, (in Chinese). DOI:10.13203/j.whugis20180333

Jiao, J., Wang, H., Dang, Y., Ren, Y., Yue, X. Wu, X., Cui, H. and Wang, X.: 2025, Noise-resilient GNSS coordinate time series prediction using AVMD-sLSTM-transformer hybrid model. Adv. Space Res., 76, 11, 6863–6881. DOI: 10.1016/j.asr.2025.09.040

Lahtinen, S., Jivall, L., Häkli, P., Kall, T., Kollo, K., Kosenko, K., Galinauskas, K., Prizginiene, D., Tangen, O. and Weber, M.: 2019, Densification of the ITRF2014 position and velocity solution in the Nordic and Baltic countries. GPS Solut., 23, 4. DOI: 10.1007/s10291-019-0886-3

Li, W. and Guo, J.: 2024, Extraction of periodic signals in Global Navigation Satellite System (GNSS) vertical coordinate time series using the adaptive ensemble empirical modal decomposition method. Nonlinear Process. Geophys., 31, 1, 99–113. DOI: 10.5194/npg-31-99-2024

Li, Z. and T. Lu.: 2025, Modeling of regional GNSS network using adaptive boosting algorithm: a case study in the Xinjiang Uyghur Autonomous Region. GPS Solut., 29, 1, 25. DOI: 10.1007/s10291-024-01780-x

Lu, T., He, J, He, X. and Tao, R.: 2023, GNSS coordinate time series denoising method based on parameter optimized variational mode decomposition. Geomat. Inf. Sci. Wuhan Univ., 49, 1856–1866, (in Chinese). DOI: 10.13203/j.whugis20220363

Lu, T., Li, Z. and He, X.: 2024, Noise-aware MEMD-XGBoost method for GNSS vertical time series modelling and prediction. J. Natl. Univ. Def. Technol., 46, 6, 149–158, (in Chinese). DOI: 10.11887/j.cn.202406016

Lu, T., Li, Z., He, X. and Zhou, S.: 2023, GNSS elevation time series prediction method based on VMD and XGBoost algorithm. Acta Geod. Cartogr. Sin., 52, 8, 1235–1244, (in Chinese). DOI: 10.11947/j.AGCS.2023.20220052

Lu, T. and Xie, J.: 2021, EEMD-Multiscale permutation entropy noise reduction method for GPS elevation time series. Geod. Geodyn., 41, 2, 111–115, (in Chinese). DOI: 10.14075/j.jgg.2021.02.001

Luo, Y., Yao, Y., Huang, C. and Zhang, Y.: 2020, Deformation feature extraction and analysis based on improved variational mode decomposition. Geomat. Inf. Sci. Wuhan Univ., 45, 612–619, (in Chinese). DOI: 10.13203/j.whugis20180286

Richman, J.S. and Moorman, J.R.: 2000, Physiological time-series analysis using approximate entropy and sample entropy. Am. J. Physiol.-Heart Circ. Physiol., 278, H2039–H2049. DOI: 10.1152/ajpheart.2000.278.6.H2039

Shi, Q.: 2023, Research on multivariate spatiotemporal Kalman filtering and its application in deformation analysis. Acta Geod. Cartogr. Sin., 52, 12, 2229, (in Chinese). DOI: 10.11947/j.AGCS.2023.20220595

Sun, F., Jia, Y., Zhu, X., Xiao, K. and Liu, J.: 2022, Advances in dynamic maintenance technology of mm-level terrestrial reference frame. Geomat. Inf. Sci. Wuhan Univ., 47, 10, 1688–1700, (in Chinese). DOI: 10.13203/j.whugis20220126

Tang, J., Li, Y. and Gao, X.: 2021, GNSS deformation monitoring denoising method based on CEEMDAN. Geod. Geodyn., 41, 4, 408–412, (in Chinese). DOI: 10.14075/j.jgg.2021.04.016

Tao, R., Lu, T. and Zhou, Z.: 2024, GNSS coordinate time series signal extraction method based on EWT and MPE. J. Geomatics Sci. Technol., 40, 5, 446–452, (in Chinese). DOI: 10.3969/j.issn.1673-6338.2024.05.002

Torres, M.E., Colominas, M.A., Schlotthauer, G. and Flandrin, P.: 2011, A complete ensemble empirical mode decomposition with adaptive noise. In: 2011 Proc. IEEE Int. Conf. Acoust. Speech Signal Process, (ICASSP), Prague, 4144–4147. DOI: 10.1109/ICASSP.2011.5947265

Wang, J., Li, Z., Fan, W., Jiang, W., Chen, Q. and Chen, H.: 2025, A new ensemble learning method based on signal source driver for GNSS coordinate time series prediction. GPS Solut., 29, 2, 68. DOI: 10.1007/s10291-025-01829-5

Wu, S., Bian, S., Li, H., Li, Z. and Ouyang, H.: 2024, Extraction of time-varying signals from GNSS height time series by variational mode decomposition. Acta Geod. Cartogr. Sin., 53, 1, 79–90, (in Chinese). DOI: 10.11947/j.AGCS.2024.20220673

Xu, K., Li, Y., Li, X., Wan, W. and Ju., H.: 2024, Seismological characteristics in the preparation process of the M7.0 Jiuzhaigou Earthquake. Geod. Geodyn., 44, 5, 497–502. DOI: 10.14075/j.jgg.2023.08.154

Yang, H., Guo, R., Zhou, J., Yang, and Sun, H.: 2022, Transient poroelastic response to megathrust earthquakes: a look at the 2015 M w 8.3 Illapel, Chile, event. Geophys. J. Int., 230, 908–915. DOI: 10.1093/gji/ggac099

Yang, H., Lu, T., Sun, X. and He, J.: 2024, GNSS coordinate time series denoising method combining SSA-VMD and wavelet decomposition. Geod. Geodyn., 44, 4, 360–365+390, (in Chinese). DOI: 10.14075/j.jgg.2023.07.105

Yang, X., Yuan, L., Jiang, Z. and Tang, M.: 2024, Joint inversion of terrestrial water storage changes in Southwest China using GNSS and GRACE/GRACE-FO data. Acta Geod. Cartogr. Sin., 53, 5, 813–822, (in Chinese). DOI: 10.11947/j.AGCS.2024.20230221

Zhang, H., Zheng, Y. and Wang, Y.: 2021, Automatic inversion of ocean internal wave parameters from SAR images based on VMD. Ocean Eng., 39, 3, 1–10. DOI: 10.11947/j.AGCS.2024.20230221

Zhang, S., Yang, Y., Xie, Y., Tang, H., Li, H., Yao, L. and Yang, Y.: 2025, GNSS signal extraction using CEEMDAN–WPD for deformation monitoring of ropeway pillars. Remote Sens., 17, 2, 224. DOI: 10.3390/rs17020224

Zhou, Y., He, X., Montillet, J.-P., Wang, Y., Hu, S., Sun, X., Huang, J. and Ma, X.: 2025, An improved ICEEMDAN-MPA-GRU model for GNSS height time series prediction with weighted quality evaluation index. GPS Solut., 29, 3, 113. DOI: 10.1007/s10291-025-01867-z

Zhu, X., Fu, Y., Cai, F. and Dai, H.: 2020, Study on the mechanism affecting nonlinear variations of GNSS station coordinates. Prog. Geophy., 35, 1, 79–85. DOI: 10.6038/pg2020CC0508